Graphene enhanced Mn-Ce binary metal oxides for catalytic oxidation and adsorption of elemental mercury from coal-fired flue gas

Yongpeng Ma[a], Bailong Mu[a], Xiaojing Zhang[a], Dongli Yuan[a], Chuang Ma[a], Haomiao Xu[b,*], Zan Qu[b], Shaoming Fang[a]

[a] Henan Collaborative Innovation Center of Environmental Pollution Control and Ecological Restoration, School of Material and Chemical Engineering, Zhengzhou University of Light Industry, No. 136, Science Avenue, Zhengzhou 450001, China
[b] School of Environmental Science and Engineering, Shanghai Jiao Tong University, Shanghai 200240, China

HIGHLIGHTS

- Novel Mn-Ce@rGO binary metal oxides was synthesized for Hg^0 removal.
- Mn-Ce@rGO composite had an excellent Hg^0 removal performance at a wide temperature window.
- CeO_2 enhanced the oxygen capture performance of the composite.

ABSTRACT

Graphene was used for the enhancement of gaseous elemental mercury (Hg^0) catalytic oxidation and adsorption over Mn-based oxides. A series of graphene modified Mn-based and Ce-Mn-based oxides were prepared via a hydrothermal method. Experimental results indicated that Mn-Ce@rGO composite has a Hg^0 removal efficiency of 91% at 250 °C which was higher than that or pure MnOx and MnOx@rGO under the same reaction conditions. Hg^0 removal efficiency decreased in the absence of O_2. The higher SO_2 concentration and space velocity resulted in lower Hg^0 removal efficiencies. The mechanism study indicated that high valances of Mn^{4+} and Mn^{3+} benefit the Hg^0 oxidation and the surface oxygen participated in the Hg^0 oxidation process. CeO_2 supplies sufficient oxygen for mercury surface adsorption. During these processes, graphene-enhanced the catalytic oxidation and adsorption processes through supporting more reaction space, facilitating electron transfer and binding sites. Moreover, the spent materials can be regenerated using a simple thermal-desorption method. Mn-Ce@rGO composite was proved to be a prospective adsorbent for Hg^0 removal from coal-fired flue gas.

1. Introduction

Mercury (Hg) has drawn a global concern due to its long persistence, high toxicity and bioaccumulation in the environment [1,2]. It is regarded as one of the most hazardous environmental contaminants [3]. Annually, approximately 2320 tons of mercury released from anthropogenic sources such as coal-fired power plants, nonferrous metal smelting plants, cement plants, etc. Among all the industrial emissions, coal-fired power plant was the biggest one [4,5]. It was estimated that approximately 40% of the total mercury emissions are derived from coal combustion [6,7]. After decades of negotiations, some global laws and regulations are formulated to control mercury emissions [8]. A famous global treaty, "*The Minamata Convention on Mercury*", was adopted on October 10, 2013, aiming at protecting human health and the environment from anthropogenic emissions [9,10]. Therefore, it is of significant to control mercury emission from anthropogenic sources.

Generally, mercury species in a coal-fired flue gas can be simply classified into three forms: elemental mercury (Hg^0), oxidized mercury (Hg^{2+}) and particle-bound mercury (Hg^p) [11,12]. Hg^p can be captured by dust removal devices such as electrostatic precipitator (ESP) and fabric filter (FF). Hg^{2+} can be effectively removed in wet flue gas desulfurization (WFGD) system due to its water solubility [13]. However, Hg^0 is of great difficulty to be captured by current contamination control technologies due to its low solubility in water and high volatility. Moreover, Hg^0 is the dominant mercury species (accounts for 66–94%) released from a coal-fired power plant [14,15]. Therefore, new technologies or novel materials for Hg^0 removal are very important for mercury removal.

Many Hg^0 removal methods were reported in literature such as adsorbents injection [11,16], Hg^0 catalytic oxidation [7,17], and some photochemical oxidation methods [18]. Among these methods, adsorption is a promising one. Carbon-based materials [19,20], metal and metal oxides [21,22], functionalized mesoporous materials [23,24], magnetic adsorbents and noble metal adsorbents [25–27] are often selected for Hg^0 capture. The surface area, pore volume and grain size play important roles during the interfaces reactions. However, most of the reported adsorbents are limited for widely utilization due to their low capacity, unrecyclable performance and high cost [28]. Activated carbon injection (ACI) is used for mercury capture due to its porous structure which can capture Hg^0, Hg^{2+} and Hg^P species. However, the high cost and low mercury capacity restrained its widespread usage in a coal-fired power plant [29]. Mesoporous materials, with the characteristic of large surface areas, high thermal and mechanical stability, ordered macro-microporous with active bonds on the surface, have been widely used as adsorbents for gaseous or aqueous contaminations [23]. In addition, some magnetic adsorbents are also widely investigated for Hg^0 capture due to their superparamagnetic and magnetic segregation properties [30]. However, the mercury adsorption capacity is low due to the physical-adsorption mechanism over mesoporous materials. Some noble metals such as platinum (Pt), gold (Au) and silver (Ag) were indicated to have Hg^0 removal capacity through an amalgamation mechanism. Ag-graphene oxide [20] and Ag-Fe [25] composites are proved to be favorable adsorbents for Hg^0. Recently, metal and metal oxides, especially some transition metal oxides, have been recognized as potential absorbents for Hg^0 [31]. Xu et al. [32] synthesized a series of one-dimensional α-, β- and γ-MnO_2 for capturing Hg^0, indicating that α-MnO_2 had the best ability for Hg^0 removal due to its large specific surface area and special crystalline structure. Moreover, a higher valence of Mn cation is important for Hg^0 oxidation. Zhou et al. [33] prepared a group of CeO_2-TiO_2 absorbents with different CeO_2/TiO_2 mass ratios and suggested that the optimum mass ratio of CeO_2/TiO_2 was 0.2, which displayed remarkable Hg^0 removal efficiencies under 80–150 °C. The high oxygen storage ability of CeO_2 endowed the Ce-Ti adsorbents with plentiful surface chemisorbed oxygen. Among these transition metal oxides, MnOx and CeOx were proved to be superior active components for Hg^0 in flue gas [34–36].

Besides, the support of adsorbent is also crucial for designing a composite. It is generally believed that the graphene was a two-dimensional single atom thick of carbon material and had further improved the performance of adsorbents due to its large specific surface area and high mechanical strength. Moreover, graphene-based materials have been widely used because of its ease of modification, and fewer harmful secondary products [37,38]. As a special carbon material, graphene oxide (GO) has been recognized as a promising support because of its hexagonal two-dimensional honeycomb structure. Reduced graphene oxide (rGO), was the reduction product of aqueous GO. In the hydrothermal reduction, the aqueous GO was assembled to form a 3D structure with a great number of interconnected pores, which provided a large surface area to active sites. Moreover, the large surface area and superior electron mobility make MnOx and CeOx uniformly dispersed on its surface or/and inset the pore of rGO avoiding the reunion of MnOx and CeOx.

Hence, in this study, a series of MnOx@rGO and Mn-Ce@rGO adsorbents were prepared to capture Hg^0 in the simulated flue gas. The adsorption experiments were conducted in a fixed-bed reaction system. The mechanism was also discussed based on the experimental and characterization results.

2. Experimental section

2.1. Preparation of rGO, MnOx@rGO and Mn-Ce@rGO

2.1.1. Synthesis of porous rGO

0.5 g of graphite powder was dispersed into 50 mL of sulfuric acid (H_2SO_4) with an ice water bath. Then, 0.5 g of sodium nitrate ($NaNO_3$) and 3 g of potassium permanganate ($KMnO_4$) were slowly added along with continuously stirring for 2 h at the temperature of 40–45 °C. Afterward, 160 mL of ultrapure water was added into the above dispersion with a 15 min continuous stirring at room temperature. Then, 10 mL of hydrogen peroxide (H_2O_2) was subsequently added, within the color change to bright yellow. Then, poured down the liquid supernatant after standing for 2 h. After that, the obtained product was rinsed with 10% hydrogen chloride via centrifugation (10,000 r·min^{-1}) to remove excess metal ions. The final precipitate was cleaned with ultrapure water via centrifugation until pH = 7. An appropriate amount of ultrapure water was added to the solution along with ultrasonically treating for 30 min, which was to peel off the oxidized graphite. Subsequently, the dispersion was centrifuged at a speed of 4000 r·min^{-1}. The GO aqueous dispersion was obtained for further use. And then, the aqueous dispersion was transferred into a Teflon-liner reaction kettle, heated at 180 °C for 12 h. The cylindrical foam was taken out and rinsed several times using ultrapure water after the reaction kettle was cooled to ambient temperature. Finally, the rGO was obtained after the freeze-dried in vacuum for 24 h.

2.1.2. Synthesis of MnOx@rGO

An amount of $MnSO_4$·H_2O was dispersed in 20 mL of ultrapure water, and then the above rGO was added in the solution and kept stirring for several minutes. The mass ratio of MnO_2:rGO was n (n = 10%, 30%, 50%). The obtained mixture was subsequently stirred for 30 min and then added an amount of NH_4·H_2O until the pH increased to about 10.0. The mixture was ultrasonically treated for 30 min after continuously stirring for another 30 min. Then, the final product was transferred into the Teflon-liner reaction kettle and treated for 12 h at 200 °C. The product was rinsed via ultrapure water several times until pH = 7. The MnOx@rGO nanomaterials were successfully constructed followed by a drying process at 60 °C.

2.1.3. Synthesis of Mn-Ce@rGO

Mn-Ce@rGO was prepared with the similar method to that of MnO_2@rGO. In this process, MnO_2 and CeO_2 where 1:1 in molar ratio, and MnO_2/CeO_2: rGO was m, where m is 10%, 30% and 50%.

2.2. Characterization of rGO, MnOx@rGO and Mn-Ce@rGO

Fourier transform infra-red (FT-IR) spectroscopy, whose excitation source was the 633 nm line of Ar^+ laser, was utilized for the detection of surface functional groups. The microstructures of the materials were analyzed using field emission scanning electron microscopy (FESEM, JSM-7001F), and the micrographs were obtained in the bright-field imaging mode at an acceleration voltage of 10.0 kV. Transmission electron microscopy (TEM, JEM-2100) was also performed to obtain the microstructures of the materials, and the samples were dispersed firstly in ethanol with strong ultra-sonication. The powder X-ray diffraction (PXRD) patterns were obtained to analyze the crystal structure of the prepared material, and the patterns were recorded on an X-ray diffractometer (DS, Advanced, Germany) with Cu Kα radiation. The scanning scale was in a 2θ range from 10° to 80° with a scanning velocity of 10°·min^{-1}. In addition, the surface elements of the materials were detected via X-ray photoelectron spectroscopy (XPS, ESCALAB 250 Xi, Thermo Fisher Scientific, USA) with a monochromatized Al Kα X-ray excitation source. And the C 1s line at 284.6 eV was taken for binding energy calibration for the detected elements.

2.3. Hg^0 removal experiments

The Hg^0 removal experiments were conducted on a bench-scale facility, which was in accordance with our previous study [17]. There are four parts included in this facility: a stimulated flue gas distributing system, a reaction system of the tubular furnace, an online detection

system and a tail gas treatment system. In this stimulated flue gas distributing system, N_2, O_2, SO_2 and Hg^0 vapor were introduced into the reaction system and N_2 was used as a carrier. Hg^0 vapor source was immersed in the thermostat water bath, which was sealed in a U-shaped glass tube. The mercury in the tube was from a mercurial thermometer, and it was transferred into the inlet of the gas mixer via passing pure N_2. 350 mL·min^{-1} total gas flow was used during the experiment procedure, which was calculated by several mass flow controllers (MFC). The Hg^0 adsorption and oxidation experiments were carried out mainly in a tubular furnace. A temperature controller in the tubular furnace could keep the system at a precise temperature. In addition, a 6 mm quartz tube in diameter (40 cm in length) was fixed in the tubular furnace where the simulated flue gas could pass through. A cold vapor atomic adsorption spectrometer (CVAAS) mercury detector was employed to analyze the online inlet and outlet Hg^0 signal. And the Hg^0 concentration was calculated by Lumex RA 915 M mercury analyzer. 6% of potassium permanganate solution was used for the oxidation of Hg^0, and active carbon was utilized for the tail gas treatment.

Before each adsorption test, the simulated flue gas containing Hg^0 vapor a firstly passed through bypass to get an initial Hg^0 signal. When the Hg^0 concentration was table, the gas was diverted to pass through the quartz tube in which contains 10 mg adsorbents (with the particle size of 40–60 meshes). The reaction temperatures were ranged from 150 to 300 °C, with the reaction time of 120 min. Besides, pure N_2, 5% O_2 and 200 ppm, 500 ppm, 1000 ppm SO_2 were chosen to investigate the influences of gas components. The 350 mL min^{-1} of gas flow rate was in accordance with a 247,700 h^{-1} of space velocity (such space velocity was higher than that of real flue gas, it can compared the Hg^0 removal performances under severe condition), and the Hg^0 inlet concentration was about 300 µg·m^{-3}.

The Hg^0 removal efficiency was calculated according to Eq. (1) as follows:

$$\text{Removal efficiency} = \frac{C_0 - C}{C_0} \times 100\% \qquad (1)$$

where the C_0 is the inlet Hg^0 concentration, and C is the outlet Hg^0 concentration.

Finally, Hg^0 temperature programmed desorption (Hg-TPD) curves were detected on the lab-scale fix-bed reactor. 10 mg of adsorbents were fixed in a quartz tube and treated by Hg^0 for 30 min at the condition of N_2 + 5% O_2 with a flow rate of 350 mL·min^{-1}. The reaction temperature was set as 250 °C. Then, O_2 was stopped and only pure N_2 was available for the Hg-TPD experiment. The temperature of the tubular furnace in this system was set from 100 to 500 °C with a heating rate of 5 °C·min^{-1}.

3. Results and discussion

3.1. Characterization of as-prepared materials

To detect the crystal structure of the as-prepared materials, XRD patterns were analyzed and the results are depicted in Fig. 1. As shown in Fig. 1, the obvious broad diffraction peaks observed at 20°–30° were attributed to the characteristic diffraction peaks of graphene [15]. For MnOx@rGO, the diffraction peaks at 18°, 28.9°, 32.3°, 36.1°, 59.8° could be attributed to (1 0 1), (1 1 2), (1 0 3), (2 1 1), (2 2 4) crystal phases of MnOx (PDF NO. 24-0734). Moreover, the diffraction peaks at 28.7°, 47.7°, 56.6° of Mn-Ce@rGO composite were marked to CeO_2 (1 1 1), CeO_2 (2 2 0) and CeO_2 (3 1 1) (PDF NO. 80-0018), respectively [36]. After MnOx and Ce-MnOx particles loaded on the surface of rGO, the oxides keep the original crystal structure.

To further investigate the morphologies of the as-prepared rGO, MnOx@rGO and Mn-Ce@rGO composites, FESEM results are displayed in Fig. 2. As shown in Fig. 2(a) and (b), the synthesized rGO has a typical nano-sheets structure. Fig. 2(c) exhibited the micrographs of MnOx@rGO composite. MnOx nanoparticles were uniformly
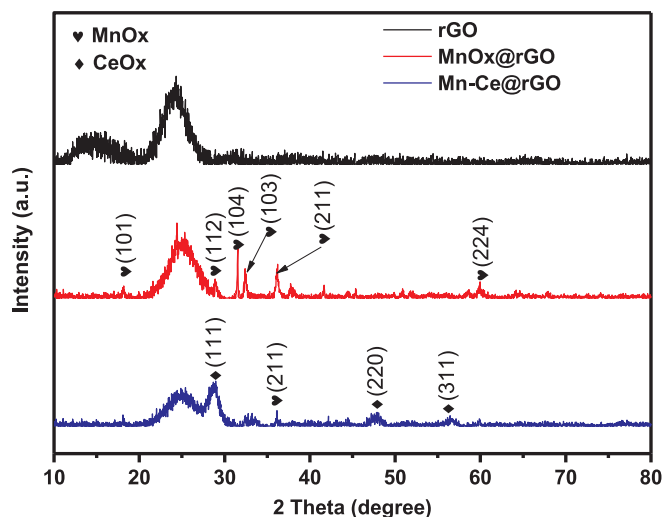

Fig. 1. Powder XRD patterns of prepared rGO, MnOx@rGO and Mn-Ce@rGO.

distributed on the surface of rGO nanosheets. Fig. 2(d) showed the photo of Mn-Ce@rGO nanocomposites, some rGO nanosheets were covered by the MnOx and CeOx nanoparticles. Mn-Ce@rGO nanocomposites formed a three-dimensional structure in which graphene acted as a good carrier for metal oxides particles. The elemental analysis of Mn-Ce@rGO via FESEM-EDX was tested and the results were shown in Fig. S2. The micrograph was obtained in the bright-field imaging mode at an acceleration voltage of 10.0 kV and the map pixel size was 0.01 µm. Like the FESEM-EDX analysis, the Ce and Mn elements are well distributed in the composite.

The TEM characterization was exhibited to analyze the microscopic morphologies of rGO, MnOx@rGO and Mn-Ce@rGO composites. The images are shown in Fig. 3. As shown in Fig. 3(a), the folds of rGO were quite thin, while rGO presents a large lamellar structure. Fig. 3(b) shows the typical TEM image of MnOx@rGO, indicating that the MnOx nanoparticles were loaded on the layer of rGO. Images of Mn-Ce@rGO are shown in Fig. 3(c) and (d), MnOx and CeOx nanoparticles grow on the surface of rGO with the functional groups. The light-gray spheres are the CeOx microspheres with an average diameter of 20 nm, and the dark regions on the rGO background are MnOx microspheres, whose average diameter was approximately 10 nm.

To identify the surface functional groups of the materials, FT-IR spectra of GO, rGO, MnOx@rGO and Mn-Ce@rGO were detected and the results are shown in Fig. 4. As shown in Fig. 4(a), the peaks centered at 1064, 1400, 1624 and 1735 cm^{-1} were attributed to the stretching vibration peaks of the alkoxy C–O, epoxy C–O, aromatic C=C and C=O, respectively [39]. And the broad adsorption band which centered at approximately 3133 cm^{-1} were correspond to vibrations of hydroxyl –OH [15]. However, some the peaks at 3133, 1064, 1400, 1624 and 1735 cm^{-1} diminished or disappeared in Fig. 4(b), (c) and (d), in the spectra of rGO, MnOx@rGO and Mn-Ce@rGO composites, indicating that these functional groups on the surface of graphene disappeared after hydrothermal process [22]. The peaks centered at 707 cm^{-1} in Fig. 4 (c) was the vibration mode of the Mn-O-C bond, confirming bonding between MnO_2 and rGO [40]. The peaks at 1207 cm^{-1} and 1559 cm^{-1} in Fig. 4(d) was assigned to the C–N stretching vibration which formed and shifted with respect to the Ce loading via adding Ce $(NO_3)_3$·H_2O and the N–H bending of –NH_2 of rGO [41,42].

According to the characterization results, the Mn-Ce@rGO composites were successfully synthesized. The three-dimensional structure of rGO was displayed and the MnOx and CeOx particles were uniformly distributed on the surface of rGO nanosheets.
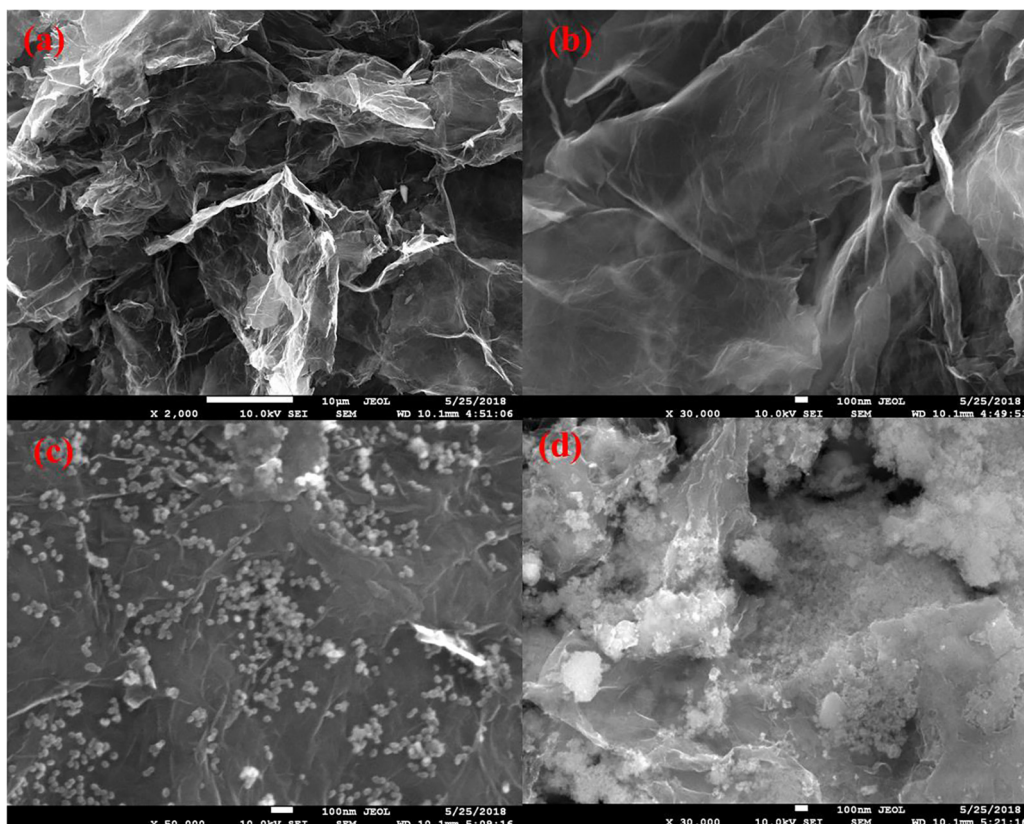
Fig. 2. FESEM patterns of (a) and (b) rGO, (c) MnOx@rGO and (d) Mn-Ce@rGO (a × 2000; b × 30,000; c × 50,000; d × 30,000).
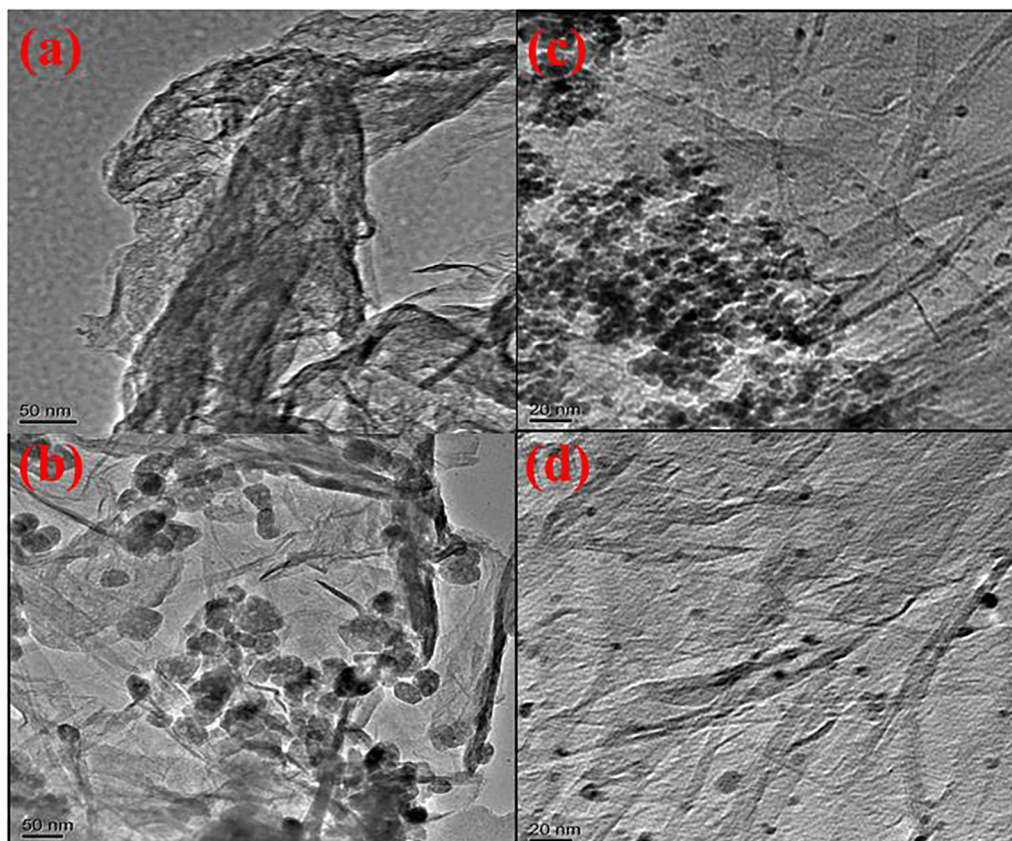

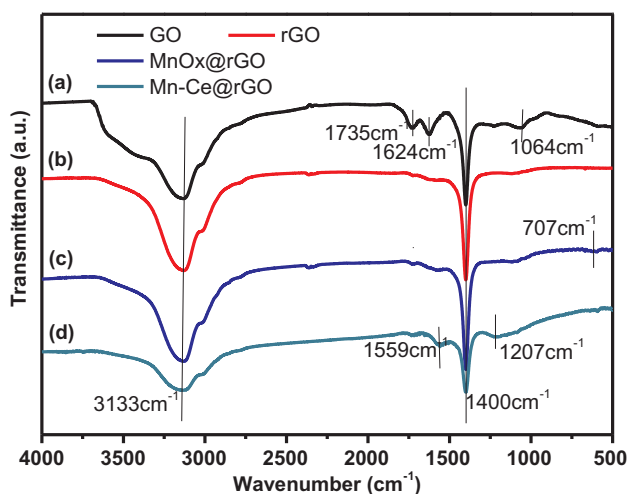**Fig. 3.** TEM images of (a) rGO, (b) MnOx@rGO, (c) and (d) Mn-Ce@rGO.

Fig. 4. FT-IR spectra of GO, rGO, MnOx@rGO and Mn-Ce@rGO.

3.2. Elemental mercury removal performances

The Hg^0 breakthrough curves of rGO, MnOx@rGO and Mn-Ce@rGO composites were tested at 250 °C and the results are shown in Fig. 5. The breakthrough curve of Mn-Ce@rGO was flat during the reaction, and the total Hg^0 removal efficiency was 91.1% in 120 min. MnOx@rGO composite was also detected for comparison. The curve began to rise slowly after a few minutes, and relegated to flat after 1 h reaction with a total Hg^0 removal efficiency of 84.8%. For rGO, it had a good removal performance in the initial few minutes, but the sharply increasing curve indicated the poorest activity for Hg^0 capture. Therefore, the Hg^0 removal efficiency of MnOx@rGO was higher than that of pure rGO.

In addition, the proportion of MnOx and MnOx/CeOx on rGO was a key factor for Hg^0 removal. The mass ratio of MnOx and MnOx/CeOx to 3D-rGO was set at 10%, 30% and 50%, and the mole ratio of MnOx: CeOx was 1:1. As exhibited in Fig. S1, these two kinds of materials had the favorable Hg^0 removal activity at a ratio of 30%. A new phenomenon occurred when the mass ratio was 50%, where the removal performance of MnOx@rGO was higher than that of Mn-Ce@rGO. The reason was that when the mass ratio was 10%, the MnOx and CeOx nanoparticles distributed on the vacancy of rGO, which provided redundant active sites. However, when the ratio was 50%, MnOx and
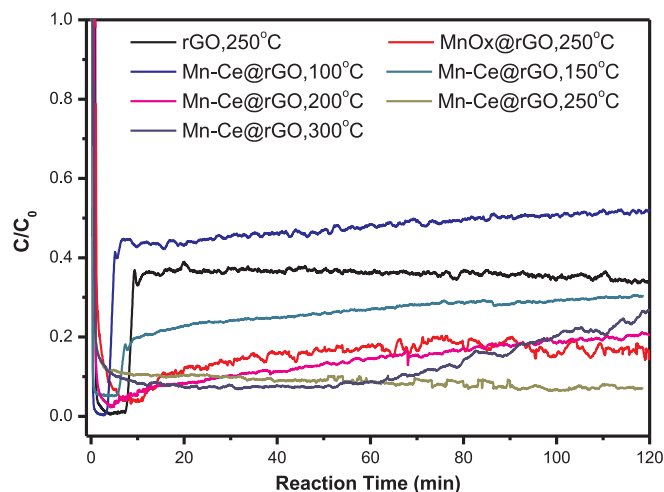

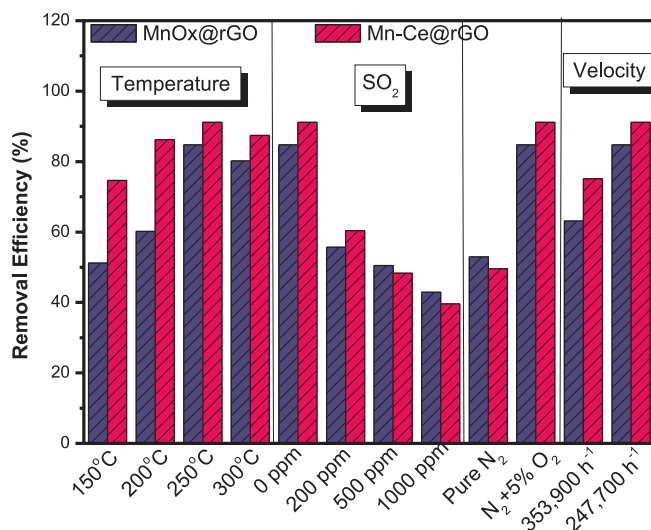**Fig. 5.** Hg^0 breakthrough curves and removal performance over rGO, MnOx@rGO and Mn-Ce@rGO.

Fig. 6. Hg^0 removal efficiency over MnOx@rGO and Mn-Ce@rGO under various conditions.

CeOx nanoparticles blocked the active sites on rGO, which led to a poor Hg^0 removal performance.

The Hg^0 removal performances over Mn-Ce@rGO at a wide temperature window (100–300 °C) were also investigated and the results are shown in Fig. 5. 300 $\mu g \cdot m^{-3}$ mercury vapor, 5% O_2 was balanced with pure N_2 with a total flow rate of 350 mL·min^{-1}. Fig. 5 showed the online data of Mn-Ce@rGO nanoparticles during 120 min, and the removal efficiency of the materials was increased with the higher reaction temperature. And it reached a peak at 250 °C with removal efficiency of 91.1%. However, when the reaction temperature was higher than 250 °C, the removal efficiency decreased and finally decreased to 87.4% at 300 °C. The Mn-Ce@rGO nanoparticles had the lowest removal efficiency at 100 °C, which was only 53.8%. Therefore, 250 °C was the optimum reaction temperature for Mn-Ce@rGO composite.

For comparison, the Hg^0 removal efficiencies of MnOx@rGO composite were provided and the results are shown in Fig. 6. From 150 to 250 °C, the removal performances increased and reached the highest value at 250 °C. Nevertheless, the removal efficiency dropped a little at 300 °C. Such tendency was similar to that of Mn-Ce@rGO composite. However, the removal performance of MnOx@rGO composite was lower than that of Mn-Ce@rGO composite.

To investigate the effect of SO_2 on Hg^0 removal over MnOx@rGO and Mn-Ce@rGO, 200, 500 and 1000 ppm SO_2 were selected in this experiment. The reaction temperature was set as 250 °C, and the reaction time was 120 min. As shown in Fig. 6, the Hg^0 removal efficiencies of MnOx@rGO and Mn-Ce@rGO were 84.8% and 91.1%, respectively. However, when 200 ppm of SO_2 was added to the simulated gas, the Hg^0 removal efficiencies decreased to 55.7% and 60.4%, respectively. When the concentration of SO_2 was set as 1000 ppm, the Hg^0 removal efficiencies decreased to 42.9% and 39.6%, respectively, indicating the poison effect of higher SO_2 concentration on Hg^0 removal. In addition, it was speculated that SO_2 and Hg^0 competitively adsorbed on MnOx adsorptive sites, limiting the Hg^0 adsorption [13,43].

To further investigate the influence of gas conditions, O_2 and space velocity were detected and depicted in Fig. 6. With the addition of 5% O_2, the Hg^0 removal efficiencies of MnOx@rGO and Mn-Ce@rGO composite increased from 52.9% and 49.6% to 84.8% and 91.9%, respectively, indicating that surface oxygen may play an important role in Hg^0 conversion.

The Hg^0 removal efficiencies over different space velocities were also studied. As shown in Fig. 6, the Hg^0 removal efficiencies decreased with the improving of space velocity over MnOx@rGO or Mn-Ce@rGO composites. At a lower space velocity as 247,700 h^{-1} and the flow rate
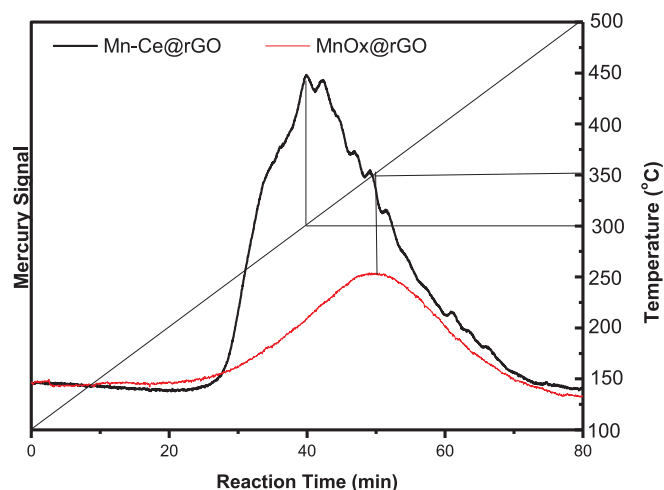
Fig. 7. Mercury desorption performances over MnOx@rGO and Mn-Ce@rGO.

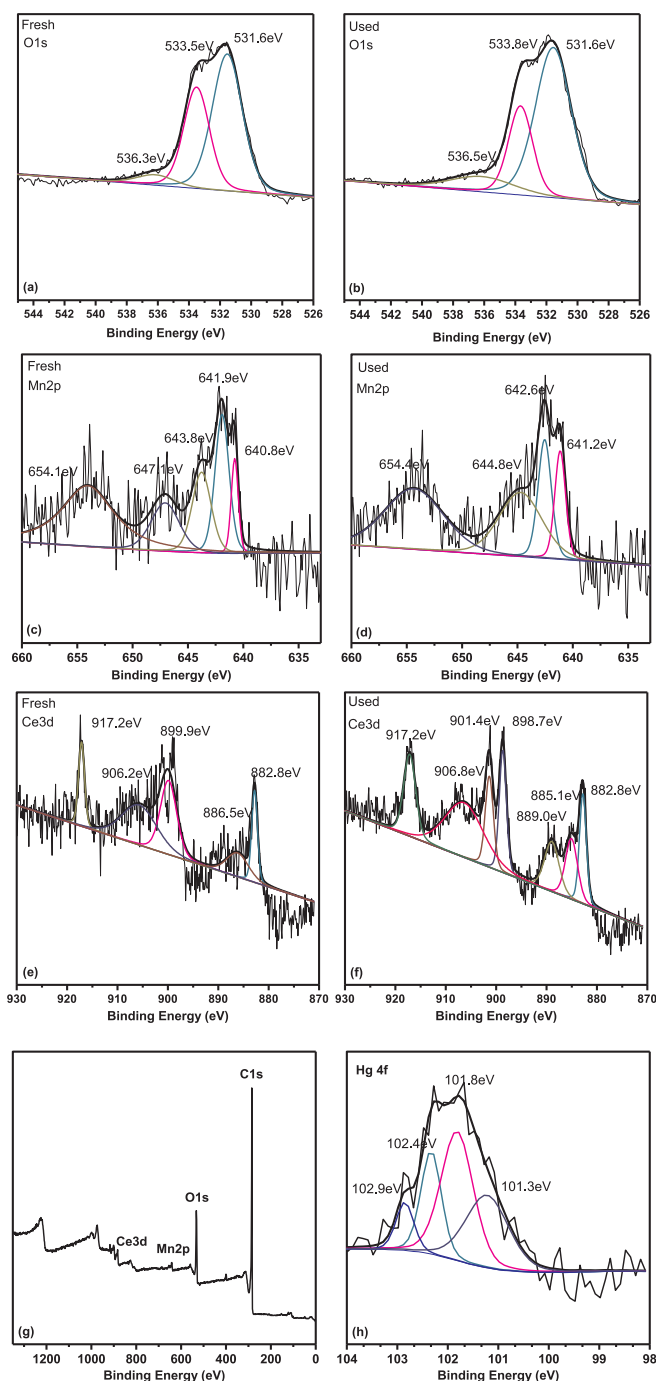**Fig. 8.** Survey XPS spectra (g) of the prepared Mn-Ce@rGO and enlarged areas corresponding to the O1s, Mn 2p, Ce 3d and Hg 4f peaks of Mn-Ce@rGO.

as 350 mL min^{-1}, the Hg^0 removal efficiency of MnOx@rGO and Mn-Ce@rGO composite reached 84.8% and 91.1%, respectively. And under the condition of with space velocity as 353,900 h^{-1} and flow rate as 500 mL min^{-1}, the efficiencies decreased to 63.1% and 75.1%, respectively. The possible reason was that the higher space velocity led to the shorter resident time of the simulated flue gas in bench-scale experimental facility.

To identify the regeneration performance of the MnOx@rGO and Mn-Ce@rGO composite after adsorption experiments, Hg-TPD was carried out and the results were shown in Fig. 7. The initial temperature of the TPD system was 100 °C with a subsequent elevated temperature to 500 °C in a heating rate of 5 °C·min^{-1}. It can be seen that Hg began to be released from the surface of MnOx@rGO and Mn-Ce@rGO at approximately 250 °C. There is peak at 300 °C, indicating that the mercury desorption got the maximum desorption rate from Mn-Ce@rGO surfce. Moreover, the desorption Hg^0 signal of Mn-Ce@rGO composite was higher than that of MnOx@rGO. The desorption curves become flat after 80 min treating, indicating that the gaseous Hg^0 approach to absolutely release from the adsorbents.

3.3. Hg^0 removal mechanism over Mn-Ce@rGO

To further explore the surface composition of the Mn-Ce@rGO composite and to better understand the Hg^0 oxidation mechanism, XPS spectra for the spectral regions of O 1s, Mn 2p, Ce 3d and Hg 4f were performed and the results are depicted as Fig. 8. The fresh and spent Mn-Ce@rGO adsorbents were both investigated for comparison. The O 1s spectra were displayed in Fig. 8(a) and (b). For fresh and spent Mn-Ce@rGO composite, the O 1s spectra were divided into three obvious peaks. The binding energy of 536.3 and 536.5 eV were attributed to surface oxygen of hydroxyl oxygen or adsorbed water. Peaks at 533.5 to 533.8 eV and 531.6 eV were ascribed to surface active oxygen and lattice oxygen, respectively. Moreover, the surface active oxygen ratio of the spent adsorbent was lower than that of the fresh sample, decreasing from 34.7% to 23.5%, indicating the participation in Hg^0 uptake process.

The XPS spectra of Mn 2p were displayed in Fig. 8(c) and (d). For fresh adsorbent, the binding energy of 654.1 eV was ascribed to Mn 2p 1/2, and the binding energy at 647.1, 643.8, 641.9 and 640.8 eV wasascribed to Mn 2p 3/2. The peaks observed at 647.1 and 643.8 eV were attributed to Mn^{4+} while 641.9 and 640.8 eV were attributed to Mn^{3+}, respectively. No peaks were attributed to Mn^{2+} in the fresh adsorbent. According to the literature [43], a higher ratio of Mn^{4+}/(Mn^{4+}/Mn^{3+}) makes a higher Hg^0 oxidation performance due to the form of MnO$_2$. In fresh adsorbent, the ratio of Mn^{4+}/(Mn^{4+} + Mn^{3+}) was 0.57, while there was no Mn^{4+} in the used, in which 642.6 and 641.2 eV were

correlated to Mn^{3+} and Mn^{2+}, respectively. The Mn^{3+} ratio in the fresh decreased from 26.6% to 16.9%, indicating that transition of Mn^{4+} to its lower valance during the reaction.

The Ce 3d XPS spectra were shown in Fig. 8(e) and (f), which consists of Ce^{4+} and Ce^{3+} in each spectrum. For the fresh sample, the binding energy at 906.2 eV was the characteristic peak of Ce^{3+}, and other four peaks belonged to Ce^{4+}. In the case of the spent sample, it was complicated with seven peaks in the pattern, in which Ce^{4+} (917.2, 901.4 and 882.8 eV), Ce^{3+} (906.8, 889.0 and 885.1 eV) and Ce^{2+} (898.7 eV) were included. This phenomenon indicated that both Ce^{4+} and Ce^{3+} were contained in the Mn-Ce@rGO adsorbent. In addition, Ce^{4+} was the prominent active component for this reaction and beneficial for Hg^0 oxidation. The ratio of Ce^{4+} decreased from 66.8% to

35.6% after using, while that of Ce^{3+} increased from 33.2% to 51.8%, suggesting that Ce^{4+} may participate in Hg^0 oxidation reaction along with the - redox reaction between Ce^{4+} and Ce^{3+}. Ce^{4+} converted to Ce^{3+} during the Hg^0 oxidation reaction, while the huge oxygen storage and release ability of Ce^{4+} enabled Ce^{3+} converting to Ce^{4+}.

Fig. 8(h) showed the Hg 4f XPS spectra of the spent adsorbent, in which the binding energy at 101.3 eV ascribed to HgO, indicating that the oxidation reaction occurred on the surface of the adsorbent. Other three peaks corresponded to Si 2p. There was no adsorbed Hg^0 on the surface of the adsorbent, since it was evaporated at a high temperature.

The Hg^0 oxidation process was attributed to the reduction of $Mn^{4+} \rightarrow Mn^{3+} \rightarrow Mn^{2+}$. In addition, the large oxygen storage ability of CeO_2 could replenish the surface oxygen [43]. With the addition of 5% O_2, the Hg^0 removal efficiency of MnOx@rGO and Mn-Ce@rGO composite was higher than that of the absence of O_2, indicating the important role of surface oxygen in Hg^0 conversion. The replenished O_2 could regenerate surface oxygen and provide chemisorbed oxygen on the surface of adsorbents, which enhanced the performance of Hg^0 oxidation.

4. Conclusions

Mn-Ce@rGO composite was successfully synthesized for Hg^0 removal from coal-fired flue gas. It had a favorable Hg^0 removal activity (approximately 91.9% during 2 h) at the temperature of 250 °C. The optimum ratio of MnOx + CeOx and rGO was 30%, and the mole ratio of MnOx: CeOx was 1:1. The results showed that SO_2 has an inhibition effect on Hg^0 removal, and the higher space velocity led to lower Hg^0 removal efficiency. However, O_2 was beneficial for the reaction. Moreover, the MnOx@rGO and Mn-Ce@rGO composites could be easily desorbed via Hg-TPD method at about 250 °C. During the adsorption process, the high valence of Mn^{4+} and Ce^{4+} enables the prominent oxidation ability for Hg^0 removal. Ce^{4+} participated in Hg^0 oxidation reaction and it was a redox reaction between Ce^{4+} and Ce^{3+}. Ce^{4+} converted to Ce^{3+} during the Hg^0 oxidation reaction, and the huge oxygen storage and release ability of Ce^{4+} enabled the conversion of Ce^{3+} to Ce^{4+}. In addition, the oxidized mercury can be released from the surface using thermal desorption method. Such a favorable Hg^0 removal performance of Mn-Ce@rGO will be a promising material for gaseous mercury purification from flue gas.

Acknowledgment

Appendix A. Supplementary data

Supplementary data to this article can be found online at https://doi.org/10.1016/j.cej.2018.10.150.

References

[1] M.P. Ancora, L. Zhang, S. Wang, J.J. Schreifels, J. Hao, Meeting Minamata: cost-effective compliance options for atmospheric mercury control in Chinese coal-fired power plants, Energy Policy 88 (2016) 485–494.

[2] L. Zhang, S. Wang, L. Wang, Y. Wu, L. Duan, Q. Wu, F. Wang, M. Yang, H. Yang, J. Hao, Updated emission inventories for speciated atmospheric mercury from anthropogenic sources in China, Environ. Sci. Technol. 49 (2015) 3185–3194.

[3] E.G. Pacyna, J.M. Pacyna, K. Sundseth, J. Munthe, K. Kindbom, S. Wilson, F. Steenhuisen, P. Maxson, Global emission of mercury to the atmosphere from anthropogenic sources in 2005 and projections to 2020, Atmos. Environ. 44 (2010) 2487–2499.

[4] Y. Ma, H. Xu, Z. Qu, N. Yan, W. Wang, Removal of mercury from flue gas from

[5] N. Pirrone, S. Cinnirella, X. Feng, R.B. Finkelman, H.R. Friedli, J. Leaner, R. Mason, A.B. Mukherjee, G.B. Stracher, D.G. Streets, Global mercury emissions to the atmosphere from anthropogenic and natural sources, Atmos. Chem. Phys. Discuss. 10 (2010) 5951–5964.

[6] Y. Wu, S. Wang, D.G. Streets, J. Hao, M. Chan, J. Jiang, Trends in anthropogenic mercury emissions in China from 1995 to 2003, Environ. Sci. Technol. 40 (2006) (1995) 5312–5318.

[7] Q. Wan, Q. Yao, L. Duan, X. Li, L. Zhang, J. Hao, Comparison of elemental mercury oxidation across vanadium and cerium based catalysts in coal combustion flue gas: catalytic performances and particulate matter effects, Environ. Sci. Technol. 52 (2018) 2981–2987.

[8] C.F. You, X.C. Xu, Coal combustion and its pollution control in China, Energy 35 (2010) 4467–4472.

[9] S. Zhao, Y. Ma, Z. Qu, N. Yan, Z. Li, J. Xie, W. Chen, The performance of Ag doped V_2O_5-TiO_2 catalyst on the catalytic oxidation of gaseous elemental mercury, Catal. Sci. Technol. 4 (2014) 2985–2993.

[10] N.E. Selin, Global change and mercury cycling: challenges for implementing a global mercury treaty, Environ. Toxicol. Chem. 33 (2014) 1202–1210.

[11] Z. Tan, L. Sun, J. Xiang, H. Zeng, Z. Liu, S. Hu, J. Qiu, Gas-phase elemental mercury removal by novel carbon-based sorbents, Carbon 50 (2012) 362–371.

[12] J.B. Milford, A. Pienciak, After the clean air mercury rule: prospects for reducing mercury emissions from coal-fired power plants, Environ. Sci. Technol. 43 (2009) 2669.

[13] H. Li, C.Y. Wu, Y. Li, L. Li, Y. Zhao, J. Zhang, Role of flue gas components in mercury oxidation over TiO_2 supported MnO_x-CeO_2 mixed-oxide at low temperature, J. Hazard. Mater. 243 (2012) 117–123.

[14] S.X. Wang, L. Zhang, G.H. Li, Y. Wu, J.M. Hao, N. Pirrone, F. Sprovieri, M.P. Ancora, Mercury emission and speciation of coal-fired power plants in China, Atmos. Chem. Phys. Discuss. 10 (2009) 1183–1192.

[15] H. Xu, Z. Qu, C. Zong, W. Huang, F. Quan, N. Yan, MnO_x/graphene for the catalytic oxidation and adsorption of elemental mercury, Environ. Sci. Technol. 49 (2015) 6823–6830.

[16] H. Xu, Q. Zan, C. Zong, F. Quan, M. Jian, N. Yan, Catalytic oxidation and adsorption of Hg^0 over low-temperature NH_3-SCR $LaMnO_3$ perovskite oxide from flue gas, Appl. Catal. B Environ. 186 (2016) 30–40.

[17] Y. Ma, B. Mu, D. Yuan, H. Zhang, H. Xu, Design of MnO_2/CeO_2-MnO_2 hierarchical binary oxides for elemental mercury removal from coal-fired flue gas, J. Hazard. Mater. 333 (2017) 186–193.

[18] E.J.G. And, H.W. Pennline, Photochemical removal of mercury from flue gas, Ind. Eng. Chem. Res. 41 (2002) 5470–5476.

[19] J. Wang, J. Yang, Z. Liu, Gas-phase elemental mercury capture by a V_2O_5/AC, Fuel Process. Technol. 91 (2010) 676–680.

[20] H. Xu, Z. Qu, W. Huang, J. Mei, W. Chen, S. Zhao, N. Yan, Regenerable Ag/graphene sorbent for elemental mercury capture at ambient temperature, Colloids Surf. A 476 (2015) 83–89.

[21] Y. Zhu, X. Han, Z. Huang, Y. Hou, Y. Guo, M. Wu, Superior activity of CeO_2 modified V_2O_5/AC catalyst for mercury removal at low temperature, Chem. Eng. J. 337 (2017) 741–749.

[22] H. Xu, Y. Yuan, Y. Liao, J. Xie, Z. Qu, W. Shangguan, N. Yan, $[MoS_4]^{2-}$ cluster bridges in Co-Fe layered double hydroxides for mercury uptake from S-Hg mixed flue gas, Environ. Sci. Technol. 51 (2017) 10109–10116.

[23] T. Cao, Z. Li, Y. Xiong, Y. Yang, S. Xu, T.M. Bisson, R. Gupta, Z. Xu, Silica-silver nanocomposites as regenerable sorbents for Hg^0 removal from flue gases, Environ. Sci. Technol. 51 (2017) 11909–11917.

[24] K. Shen, L. Zhang, X. Chen, L. Liu, D. Zhang, Y. Han, J. Chen, J. Long, R. Luque, Y. Li, Ordered macro-microporous metal-organic framework single crystals, Science 359 (2018) 206.

[25] L. Dong, J. Xie, G. Fan, Y. Huang, J. Zhou, Q. Sun, L. Wang, Z. Guan, D. Jiang, Y. Wang, Experimental and theoretical analysis of element mercury adsorption on Fe3O4/Ag composites, Korean J. Chem. Eng. 34 (2017) 2861–2869.

[26] S. Zhao, D. Chen, H. Xu, J. Mei, Z. Qu, P. Liu, Y. Cui, N. Yan, Combined effects of Ag and UiO-66 for removal of elemental mercury from flue gas, Chemosphere 197 (2018) 65–72.

[27] D.H. Lim, S. Aboud, J. Wilcox, Investigation of adsorption behavior of mercury on Au(111) from first principles, Environ. Sci. Technol. 46 (2012) 7260–7266.

[28] S. Yang, Y. Guo, N. Yan, Z. Qu, J. Xie, C. Yang, J. Jia, Capture of gaseous elemental mercury from flue gas using a magnetic and sulfur poisoning resistant sorbent Mn/γ-Fe2O3 at lower temperatures, J. Hazard. Mater. 186 (2011) 508–515.

[29] S. Sjostrom, M. Durham, C.J. Bustard, C. Martin, Activated carbon injection for mercury control: overview, Fuel 89 (2010) 1320–1322.

[30] K. Liang, X.J. Qiao, Z.G. Sun, X.D. Guo, L. Wei, Y. Qu, Preparation and microwave absorbing properties of graphene oxides/ferrite composites, Appl. Phys. A 123 (2017) 445.

[31] S. Yang, N. Yan, Y. Guo, D. Wu, H. He, Z. Qu, J. Li, Q. Zhou, J. Jia, Gaseous elemental mercury capture from flue gas using magnetic nanosized $(Fe_3-xMnx)1-\delta O_4$, Environ. Sci. Technol. 45 (2011) 1540.

[32] H. Xu, Q. Zan, S. Zhao, M. Jian, F. Quan, N. Yan, Different crystal-forms of one-dimensional MnO_2 nanomaterials for the catalytic oxidation and adsorption of elemental mercury, J. Hazard. Mater. 299 (2015) 86–93.

[33] J. Zhou, W. Hou, P. Qi, X. Gao, Z. Luo, K. Cen, CeO_2-TiO_2 sorbents for the removal of elemental mercury from syngas, Environ. Sci. Technol. 47 (2013) 10056–10062.

[34] H. Xu, N. Yan, Z. Qu, W. Liu, J. Mei, W. Huang, S. Zhao, Gaseous heterogeneous catalytic reactions over Mn-based oxides for environmental applications–a critical review, Environ. Sci. Technol. 51 (2017) 8879.

[35] Y. Gao, Z. Zhang, J. Wu, L. Duan, A. Umar, L. Sun, Z. Guo, Q. Wang, A critical review on the heterogeneous catalytic oxidation of elemental mercury in flue gases, Environ. Sci. Technol. 47 (2013) 10813–10823.

[36] C. He, B. Shen, J. Chen, J. Cai, Adsorption and oxidation of elemental mercury over Ce-MnOx/Ti-PILCs, Environ. Sci. Technol. 48 (2014) 7891–7898.

[37] Y. Yang, M. Kang, S. Fang, M. Wang, L. He, J. Zhao, H. Zhang, Z. Zhang, Electrochemical biosensor based on three-dimensional reduced graphene oxide and polyaniline nanocomposite for selective detection of mercury ions, Sens. Actuators, B 214 (2015) 63–69.

[38] Y. Chen, X. Song, T. Zhao, Y. Xiao, Y. Wang, X. Chen, A phosphorylethanolamine-functionalized super-hydrophilic 3D graphene-based foam filter for water purification, J. Hazard. Mater. 343 (2017) 298–303.

[39] M. Hu, K.S. Hui, K.N. Hui, Role of graphene in MnO₂/graphene composite for

catalytic ozonation of gaseous toluene, Chem. Eng. J. 254 (2014) 237–244.

[40] J. Li, N. Yan, Z. Qu, S. Qiao, S. Yang, Y. Guo, P. Liu, J. Jia, Catalytic oxidation of elemental mercury over the modified catalyst Mn/α-Al2O3 at lower temperatures, Environ. Sci. Technol. 44 (2009) 426–431.

[41] J. Luo, Y. Xu, W. Yao, C. Jiang, J. Xu, Synthesis and microwave absorption properties of reduced graphene oxide-magnetic porous nanospheres-polyaniline composites, Compos. Sci. Technol. 117 (2015) 315–321.

[42] L. Zhang, H. Luo, P. Liu, W. Fang, J. Geng, A novel modified graphene oxide/chitosan composite used as an adsorbent for Cr(VI) in aqueous solutions, Int. J. Biol. Macromol. 87 (2016) 586–596.

[43] Y. Wang, B. Shen, C. He, S. Yue, F. Wang, Simultaneous removal of NO and Hg⁰ from flue gas over Mn-Ce/Ti-PILCs, Environ. Sci. Technol. 49 (2015) 9355–9936.